A double layer-averaged model for dam-break flows over mobile bed

PhD Student Ji Li[a], Zhixian Cao Professor[bc], Gareth Pender (IAHR Member), Professor[de] & Qingquan Liu Professor[f]

[a] State Key Laboratory of Water Resources and Hydropower Engineering ScienceWuhan University, Wuhan, People's Republic of China

[b] State Key Laboratory of Water Resources and Hydropower Engineering Science, Wuhan University, Wuhan, People's Republic of China

[c] Institute for Infrastructure and Environment, Heriot-Watt University, Edinburgh, UK

[d] Institute for Infrastructure and Environment, Heriot-Watt University, Edinburgh, UK

[e] State Key Laboratory of Water Resources and Hydropower Engineering Science, Wuhan University, Wuhan, People's Republic of China

[f] Institute of Mechanics, Chinese Academy of Sciences, Beijing, People's Republic of China
Published online: 25 Aug 2013.

PLEASE SCROLL DOWN FOR ARTICLE

Research paper

A double layer-averaged model for dam-break flows over mobile bed

JI LI, PhD Student, *State Key Laboratory of Water Resources and Hydropower Engineering Science, Wuhan University, Wuhan, People's Republic of China*
Email: 2008301580283@whu.edu.cn

ZHIXIAN CAO, Professor, [a]*State Key Laboratory of Water Resources and Hydropower Engineering Science, Wuhan University, Wuhan, People's Republic of China; Professor, [b]Institute for Infrastructure and Environment, Heriot-Watt University, Edinburgh, UK*
Email: zxcao@whu.edu.cn (author for correspondence)

GARETH PENDER (IAHR Member), Professor, [a]*Institute for Infrastructure and Environment, Heriot-Watt University, Edinburgh, UK; Visiting Professor, [b]State Key Laboratory of Water Resources and Hydropower Engineering Science, Wuhan University, Wuhan, People's Republic of China*
Email: g.pender@hw.ac.uk

QINGQUAN LIU, Professor, *Institute of Mechanics, Chinese Academy of Sciences, Beijing, People's Republic of China*
Email: qqliu@imech.ac.cn

ABSTRACT
Dam-break flows over mobile bed are often sharply stratified, comprising a bedload sediment-laden layer and an upper clear-water layer. Double layer-averaged (DL) models are attractive for modelling such flows due to the balance between the computing cost and the ability to represent stratification. However, existing DL models are oversimplified as sediment concentration in the sediment-laden layer is presumed constant, which is not generally justified. Here a new DL model is presented, explicitly incorporating the sediment mass conservation law in lieu of the assumption of constant sediment concentration. The two hyperbolic systems of the governing equations for the two layers are solved separately and simultaneously. The new model is demonstrated to agree with the experimental measurements of instant and progressive dam-break floods better than a simplified double layer-averaged model and a single layer-averaged model. It shows promise for applications to sharply stratified sediment-laden flows over mobile bed.

Keywords: Dam break; flood; layer-averaged model; sediment-laden flow; shallow flow

1 Introduction

Dam-break flows are generally energetic and induce active sediment transport and morphological changes, which in turn conspire to modify the flows. In general, strong interactions exist between the flow, sediment transport and channel morphology. Since the pioneering work of Capart and Young (1998), laboratory experiments have contributed significantly to the understanding of dam-break hydraulics over mobile bed (Spinewine 2005a, Cao *et al.* 2011a, 2011b, Schmocker and Hager 2012). However, flume experiments are usually constrained by the comparatively small spatial scales in laboratories and may not be sufficient for fully unraveling the complex mechanisms of dam-break flows. Computational study is an attractive alternative for

enhancing the understanding of mobile bed dam-break flows. Indeed, the work of Capart and Young (1998) acted as a catalyst for the development of many numerical models (Cao *et al.* 2004, 2011a, 2011c, Spinewine 2005a, Leal *et al.* 2006, 2010a, 2010b, Spinewine and Zech 2007, Wu and Wang 2007, Xia *et al.* 2010, Goutière *et al.* 2011, Soares-Frazão *et al.* 2012).

Most mathematical models for dam-break flows to date are single layer-averaged (SL) models based on conventional shallow water hydrodynamic principles (Capart and Young 1998, Cao *et al.* 2004, Wu and Wang 2007, Leal *et al.* 2010a, 2010b, Xia *et al.* 2010). However, dam-break induced sediment-laden flows can be sharply stratified, which means the flow comprises a bedload sediment-laden flow layer immediately over the bed and an upper clear-water flow layer (Capart and Young 1998).

A two-phase flow model is appealing for modelling such flows (Greco *et al.* 2012), as the inter-phase interactions are explicitly represented. More distinctively, as underpinned by the sharply stratified structure of such flows, double layer-averaged (DL) models have been proposed (Fraccarollo and Capart 2002, Capart and Young 2002, Spinewine 2005a, 2005b, Savary and Zech 2007, Zech *et al.* 2008). This is sensible because the computing cost is significantly reduced compared with a vertical 2D or full 3D model that fully resolves the vertical flow structure, and equally importantly the stratification of the flow is reasonably represented, which however is normally ignored in a SL model. Yet, existing DL models are oversimplified because sediment concentration in the bedload transport layer is presumed constant. For highly unsteady and varied dam-break flows, this assumption is far from generally justified. In principle, sediment concentration is one of the unknowns to be solved by a numerical model, but in existing simplified double layer-averaged (SDL) models (Spinewine 2005a, 2005b, Savary and Zech 2007, Zech *et al.* 2008, 2009), its value needs to be specified a priori and thus uncertainty is introduced inevitably. Succinctly, from a physical point of view, the fundamental mass conservation law for sediment is violated. The consequence of this can be serious. For example, according to Fraccarollo and Capart (2002), sediment particle size would have no effect on the bed scour induced by dam-break flows, which is questionable from physical intuition. Most plausibly, this stems from the assumption of constant sediment concentration, though the impact of the assumed equal velocities of the two layers is not precluded. Indeed, the extended models by, for instance, Capart and Young (2002), Spinewine (2005a) and Zech *et al.* (2009) do not involve the assumption of equal velocity in the two layers. It is also noted that Chen and Peng (2006) and La Rocca *et al.* (2012) have developed DL models for stratified flows of different densities. However, these models are applicable for shallow flows over fixed bed, without accounting for sediment transport and morphological evolution, which are key features of dam-break flows over mobile bed.

This paper presents a physically enhanced DL model for dam-break flow, sediment transport and morphological evolution. It is built upon the mass and momentum conservation laws for each layer closed with relationships representing the interface and bed shear stresses, the inter-layer mass exchange

flux and sediment exchange fluxes with the bed. This model is new as the assumption of constant sediment concentration embedded in existing DL models is eliminated. Within the new model, the governing equations for each layer are cast into a non-homogeneous hyperbolic system, whilst the interactions between the two layers and between the lower layer and the mobile bed, the boundary resistance and gravitational action are represented as source terms. The two systems for the two layers are solved separately and simultaneously. For each hyperbolic system, an operator-splitting framework is employed. The total-variation-diminishing version (TVD) of the second-order weighted-average-flux (WAF) method is used along with the HLL (Harten–Lax–van Leer) and HLLC (Harten–Lax–van Leer contact wave) approximate Riemann solvers for the homogeneous equations. A Runge–Kutta scheme is applied to solve the ordinary differential equations composed of the source terms. The new model is tested against a series of cases, including laboratory experiments on flows induced by instant and full dam break (Spinewine 2005a) and also flows due to progressive failure of a single and cascade landslide dams (Cao *et al.* 2011a, 2011b, Schmocker and Hager 2012). The model has also been compared with two existing models, including the SDL model of Spinewine (2005a) and the SL model by Cao *et al.* (2004).

2　Mathematical model

2.1　*Structure of the DL model*

A general sketch of the DL model is presented in Fig. 1. The system comprises two moving layers and one layer at rest. Specifically, these are (1) an upper clear-water flow layer of depth h_w and layer-averaged velocity u_w; (2) a lower sediment-laden flow layer of depth h_s, layer-averaged velocity u_s and volumetric sediment concentration C_s; and (3) a mobile bed of volumetric sediment concentration C_b with vanishing velocity. The upper layer interacts with the lower layer by exchanging clear water, but the lower layer also exchanges water and sediment with the mobile bed. In Fig. 1, E and D are the sediment entrainment and deposition fluxes across the bottom boundary, respectively; E_w is the mass exchange flux of clear water across the interface between the two layers; η the stage and z_b the bed elevation.
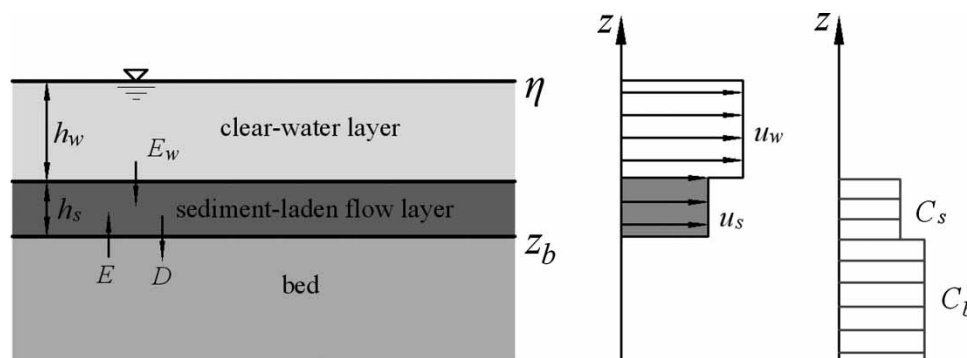

Figure 1　Structure of DL models

2.2 *Governing equations*

Consider longitudinally one-dimensional dam-break flows over mobile bed composed of uniform and non-cohesive sediment with particle diameter d. The governing equations of a DL model comprise the mass and momentum conservation equations, respectively, for the clear-water flow layer and the sediment-laden flow layer, and also the mass conservation equations for, respectively, the sediment in the lower layer and bed sediment (see Fig. 1). These equations can be derived from the fundamental conservation laws in fluid dynamics (Batchelor 1967) under the framework of shallow water hydrodynamics (Wei 1990), and can be written as

$$\frac{\partial h_w}{\partial t} + \frac{\partial h_w u_w}{\partial x} = -E_w \tag{1}$$

$$\frac{\partial h_w u_w}{\partial t} + \frac{\partial}{\partial x}\left(h_w u_w^2 + \frac{1}{2}gh_w^2\right)$$
$$= -\frac{\tau_w}{\rho_w} - gh_w\frac{\partial(z_b + h_s)}{\partial x} - E_w u_w \tag{2}$$

$$\frac{\partial h_s}{\partial t} + \frac{\partial h_s u_s}{\partial x} = E_w + \frac{E - D}{1 - p} \tag{3}$$

$$\frac{\partial h_s u_s}{\partial t} + \frac{\partial}{\partial x}\left(h_s u_s^2 + \frac{1}{2}gh_s^2\right)$$
$$= \frac{\tau_w - \tau_b}{\rho_c} - gh_s\frac{\partial z_b}{\partial x} - \frac{\rho_w g}{\rho_c}h_s\frac{\partial h_w}{\partial x} - \frac{(\rho_0 - \rho_c)(E - D)u_s}{(1 - p)\rho_c}$$
$$+ \frac{(\rho_s - \rho_w)C_s E_w u_s}{\rho_c} + \frac{\rho_w E_w u_w}{\rho_c} - \frac{(\rho_s - \rho_w)gh_s^2}{2\rho_c}\frac{\partial C_s}{\partial x} \tag{4}$$

$$\frac{\partial h_s C_s}{\partial t} + \frac{\partial h_s u_s C_s}{\partial x} = E - D \tag{5}$$

$$\frac{\partial z_b}{\partial t} = -\frac{E - D}{1 - p} \tag{6}$$

where t is the time; x the streamwise coordinate; g the gravitational acceleration; $p = 1 - C_b$ the bed sediment porosity; ρ_w and ρ_s are the densities of water and sediment, respectively; $\rho_c = \rho_w(1 - C_s) + \rho_s C_s$ is the density of the water–sediment mixture in the sediment-laden flow layer; $\rho_0 = \rho_w p + \rho_s(1 - p)$ the density of the saturated bed; τ_w the shear stress at the interface between the two layers; and τ_b the bed shear stress.

Equations (1) and (2) represent the mass and momentum conservation equations for the clear-water layer. The first two terms on the right hand side (RHS) of Eq. (2) represent the interfacial resistance and gravity acting on this layer, and the third term on its RHS illustrates the momentum transfer due to clear water exchange across the interface. Equation (3) describes the mass conservation equation for the sediment-laden flow layer. The second term on its RHS quantifies the contribution of the mass exchange with the bed. Equation (4) represents momentum conservation for the water–sediment mixture flow in the lower layer. The first three terms on its RHS represent, respectively, the interfacial and bed resistances, gravity and hydrostatic pressure of

the clear-water layer acting on the lower layer. The fourth term on its RHS represents the momentum transfer due to sediment exchange with the bed. Likewise, the fifth and sixth terms on its RHS represent the momentum transfer arising from clear water exchange between two moving layers. The last term on its RHS indicates the contribution of the spatial variations in sediment concentration. Equation (5) represents the sediment mass conservation in the lower layer, incorporating sediment exchange with the bed. Equation (6) indicates the bed deformation rate.

2.3 *Comparison with existing models*

Under certain premises, the DL model degenerates into two existing dam-break flow models, i.e. the SL model (Cao *et al.* 2004) and SDL model (Spinewine 2005a). First, when the clear-water layer vanishes and in line with this status there is no water exchange across the interface, Eqs. (1) and (2) are trivial and Eqs. (3)–(6) become the same as those of the SL model of Cao *et al.* (2004).

Second, if sediment concentration C_s in the lower layer is assumed constant as in the SDL model by Spinewine (2005a), Eq. (5) is no longer required. When e_b is introduced to quantify the bed erosion rate, instead of the sediment fluxes in Eq. (6), bed evolution is quantified by

$$\frac{\partial z_b}{\partial t} = -e_b \tag{7}$$

A relationship between e_b and E_w is suggested by Spinewine (2005a), i.e.

$$E_w = e_b\frac{C_b - C_s}{C_s} \tag{8}$$

By substituting Eqs. (7) and (8) into the governing equations of the DL model, one obtains the governing equations of the SDL model due to Spinewine (2005a). For the clear-water layer

$$\frac{\partial h_w}{\partial t} + \frac{\partial h_w u_w}{\partial x} = -e_b\frac{C_b - C_s}{C_s} \tag{9}$$

$$\frac{\partial h_w u_w}{\partial t} + \frac{\partial}{\partial x}\left(h_w u_w^2 + \frac{1}{2}gh_w^2\right) = -\frac{\tau_w}{\rho_w} - gh_w\frac{\partial(z_b + h_s)}{\partial x}$$
$$- e_b\frac{C_b - C_s}{C_s}u_w \tag{10}$$

and for the sediment-laden flow layer

$$\frac{\partial h_s}{\partial t} + \frac{\partial h_s u_s}{\partial x} = e_b\frac{C_b - C_s}{C_s} + e_b = e_b\frac{C_b}{C_s} \tag{11}$$

$$\frac{\partial h_s u_s}{\partial t} + \frac{\partial}{\partial x}\left(h_s u_s^2 + \frac{1}{2}gh_s^2\right)$$
$$= \frac{\tau_w - \tau_b}{\rho_c} - gh_s\frac{\partial z_b}{\partial x} - \frac{\rho_w g}{\rho_c}h_s\frac{\partial h_w}{\partial x} + e_b u_w\frac{C_b - C_s}{C_s}\frac{\rho_w}{\rho_c} \tag{12}$$

2.4　*Model closure*

To close the governing equations of the DL model, a set of relationships has to be introduced to determine the boundary resistance, interface shear stress, the clear water exchange flux between the two layers, and the sediment exchange flux between the lower layer and the bed. Generally, unsteady and non-uniform dam-break flows may experience boundary resistances substantially different from those of steady and uniform flows. This is more pronounced when sediment transport occurs, which renders the bed movable and bedforms generated. However, no generally applicable relationships are currently available to represent boundary resistance in such flows. Consequently, computational studies of dam-break floods over fixed and mobile beds continue to use resistance relationships initially developed for steady and uniform flows, such as the Manning's equation. This practice is followed for the present DL model by virtue of the conventional empirical relationships

$$\tau_w = \frac{\rho_w g n_w^2 (u_w - u_s)^2}{h_w^{1/3}} \tag{13}$$

$$\tau_b = \frac{\rho_c g n_b^2 u_s^2}{h_s^{1/3}} \tag{14}$$

where n_w is the roughness at the interface between the upper and lower layers; and n_b is the roughness of the bed.

A slightly adapted version of the relationship initially proposed for turbidity currents (Parker *et al.* 1987) is tentatively used for determining E_w

$$E_w = -e_w(u_s - u_w) \tag{15}$$

where the exchange coefficient e_w is calculated empirically using the Richardson number $Ri = sgC_s h_s/(u_w - u_s)^2$ and specific gravity of sediment $s = \rho_s/\rho_w - 1$

$$e_w = \frac{0.00153}{0.0204 + Ri} \tag{16}$$

Generally, two distinct mechanisms are involved in sediment exchange with the bed, i.e. bed sediment entrainment due to turbulence and sediment deposition by gravitational action, though sediment particle–particle interactions may modify the exchange to some extent. The determination of the entrainment and deposition fluxes continues to be one of the pivotal components of computational models for fluvial sediment transport and morphological evolution. Nonetheless, current formulations hinge upon a series of assumptions, which are briefly reviewed in Cao and Carling (2002). There is little dispute that the deposition flux can be determined practically by using the local near-bed sediment concentration and hindered settling velocity. One of the most widely used approaches to specifying bed sediment entrainment flux is based on the assumption that entrainment always occurs at the same rate as it does under capacity regime.

In capacity conditions, the entrainment flux is equal to the deposition flux. Therefore, the bed sediment entrainment flux can be computed by using near-bed sediment concentration at capacity and hindered settling velocity. Typically, bedload sediment concentration varies very little vertically within the lower layer, as compared with its longitudinal variation. Thus, the near-bed concentration can be represented by the average concentration of the lower layer. Accordingly, the entrainment and deposition fluxes are estimated by

$$E = \omega c_e (1 - c_e)^m, \quad D = \omega C_s (1 - C_s)^m \tag{17}$$

where ω is the settling velocity of a single sediment particle in tranquil clear water, calculated using Zhang's formula (Zhang and Xie 1993); and hindered sediment settling velocity is taken into account using the relationship of Richardson and Zaki (1954), where $m = 4.45 R_p^{-0.1}$, $R_p = \omega d/\nu$ is the particle Reynolds number and ν the kinematic viscosity of water. The bedload sediment transport capacity c_e is determined by

$$c_e = \frac{q_b}{h_s u_s}, \quad q_b = \Phi 8\sqrt{sgd^3}(\theta - \theta_c)^{1.5} \tag{18}$$

where q_b is the unit-width bedload transport rate at transport capacity status; ϕ the modification coefficient; $\theta = u_*^2/(sgd)$ the Shields parameter; u_* the friction velocity and θ_c the critical Shields parameter for initiation of sediment movement. Usually, the threshold Shields parameter can be empirically determined over sufficiently mild slopes using the Shields diagram (Chien and Wan 1999). Yet, for dam-break processes that may feature steep slopes, θ_c is determined following Cao *et al.* (2011c). Although a plethora of empirical formulations is available for calculating q_b, they are derived under steady and uniform flows, and therefore the entrainment flux based on these formulations may not be directly applicable to dam-break flows. A slightly modified version of the MPM (Meyer-Peter and Müller 1948) formula is introduced here (MMPM: Modified MPM), with a modification coefficient ϕ to be calibrated using measured data. This is necessary as the Shields parameter in dam-break floods can go far beyond the range in which the MPM formula was initially derived. In essence, it is a functional form of bedload transport rate introduced based on the MPM formula, especially when the modification by Wong and Parker (2006) is considered.

In the present work, the closure relationships for the SL model are in principle the special version of those for the DL model as the upper clear-water flow layer vanishes. To close the SDL model, an empirical relationship is proposed to directly determine the bed erosion rate e_b using a lower and upper value of the shear stress at the bed (Spinewine 2005a), instead of the entrainment and deposition fluxes in Eq. (17).

Mathematical modelling has become one of the most proactive approaches in the context of hydraulic research and engineering practice. Yet concerns over its reliability remain, especially when sediment transport and morphological evolution are involved. One of the most viable strategies to address

these concerns is to incorporate in the governing equations of a model as much physics as possible and thereby minimize its uncertainty (uncertainty is inevitable because of the empirical relationships introduced to close the model). The present work is just one example with respect to this philosophy, i.e. eliminating the assumption of constant sediment concentration in the lower layer in SDL models by applying the fundamental mass conservation law for sediment, i.e. Eq. (5). It is this fact that distinguishes the present DL model from the existing SDL model (Spinewine 2005a). Equally importantly, this must not be confused with the empirical relationships introduced to close the governing equations of the models, which are far from universally applicable and inevitably feature uncertainty. The latter fact certainly necessitates systematic, fundamental investigations of the mechanisms of sediment transport in complex flows, i.e. highly unsteady and rapidly varied flows. Before new established closure formulations are available, it has to be dealt with by empiricism that can be accrued through practice using measured datasets.

2.5 *Numerical algorithm*

There have been analyses of DL models for clear-water flows over fixed bed, without involving sediment transport or mobile bed. If the difference of the velocities of the two layers exceeds a threshold, the system of the governing equations as a whole loses hyperbolicity and Kelvin–Helmholtz instability is expected (Kim and LeVeque 2008), though an explicit expression for the eigenvalues of the DL system is unavailable. Succinctly, the loss of hyperbolicity has implications for the selection of numerical algorithms for solving the equations and the implementation of boundary conditions. Accordingly, a special treatment has to be developed. The introduction of an intermediate third layer seems viable for recovering hyperbolicity (Castro *et al.* 2010). Nevertheless, Eqs. (1)–(6) constitute a nonlinear system of six partial differential equations, involving more equations than analysed previously (Kim and LeVeque 2008, Castro *et al.* 2010). It is too complicated to be solved numerically as a single system presently, which is reserved for future studies.

Given the above observation, an alternative solution strategy has to be developed. As bed deformation is entirely determined by local entrainment and deposition fluxes under the non-capacity framework for sediment transport, Eq. (6) is separated from the remaining equations and can be readily solved. Furthermore, from a physical perspective, it is proposed that either the upper clear-water flow layer or the lower sediment-laden flow layer is dictated by its own inertia, gravity and boundary resistance, whilst the inter-layer interactions (mainly the second term on the RHS of Eq. 2 and the third term on the RHS of Eq. 4) play a secondary role and can therefore be set as source terms in the momentum equations. In fact, the inter-layer interactions can be confirmed to be negligible post priori, i.e. after the numerical solution of a specific case has been achieved.

The above solution strategy facilitates the decomposition of Eqs. (1)–(5) to two reduced-order systems that represent the upper clear-water flow layer and the lower sediment-laden flow layer, respectively. The two systems can be readily proved to be hyperbolic and are much easier to solve than the single system of Eqs. (1)–(5), i.e.

$$\frac{\partial \boldsymbol{T}}{\partial t} + \frac{\partial \boldsymbol{E}}{\partial x} = \boldsymbol{R} \tag{19}$$

$$\frac{\partial \boldsymbol{U}}{\partial t} + \frac{\partial \boldsymbol{F}}{\partial x} = \boldsymbol{S} \tag{20}$$

$$\boldsymbol{T} = \begin{bmatrix} h_w \\ h_w u_w \end{bmatrix} \tag{21a}$$

$$\boldsymbol{E} = \begin{bmatrix} h_w u_w \\ h_w u_w^2 + \frac{1}{2} g h_w^2 \end{bmatrix} \tag{21b}$$

$$\boldsymbol{R} = \begin{bmatrix} e_w(u_s - u_w) \\ -\frac{\tau_w}{\rho_w} - g h_w \frac{\partial(z_b + h_s)}{\partial x} + e_w(u_s - u_w)u_w \end{bmatrix} \tag{21c}$$

$$\boldsymbol{U} = \begin{bmatrix} h_s \\ h_s u_s \\ h_s C_s \end{bmatrix} \tag{22a}$$

$$\boldsymbol{F} = \begin{bmatrix} h_s u_s \\ h_s u_s^2 + \frac{1}{2} g h_s^2 \\ h_s u_s C_s \end{bmatrix} \tag{22b}$$

$$\boldsymbol{S} = \begin{bmatrix} -e_w(u_s - u_w) + \frac{E-D}{1-p} \\ M_0 \\ E - D \end{bmatrix} \tag{22c}$$

$$M_0 = \frac{\tau_w - \tau_b}{\rho_c} - g h_s \frac{\partial z_b}{\partial x} - \frac{\rho_w g}{\rho_c} h_s \frac{\partial h_w}{\partial x} - \frac{(\rho_0 - \rho_c)(E-D)u_s}{(1-p)\rho_c}$$
$$- \frac{(\rho_s - \rho_w)C_s u_s e_w(u_s - u_w)}{\rho_c} - e_w(u_s - u_w)u_w \frac{\rho_w}{\rho_c}$$
$$- \frac{(\rho_s - \rho_w)g h_s^2}{2\rho_c} \frac{\partial C_s}{\partial x} \tag{22d}$$

where $\boldsymbol{T}$ and $\boldsymbol{U}$ are the conserved variables; $\boldsymbol{E}$ and $\boldsymbol{F}$ are the flux variables; $\boldsymbol{R}$ and $\boldsymbol{S}$ are the source terms for the clear-water flow layer and the sediment-laden flow layer, respectively.

Equations (19) and (20) constitute two non-homogeneous hyperbolic systems and can be solved separately and simultaneously using one of a hierarchy of numerical algorithms that can capture shock waves and contact discontinuities properly (Toro 2001, LeVeque 2002). Take Eq. (20) as an example, a standard splitting algorithm (Toro 2001) is employed

$$\boldsymbol{U}_i^q = \boldsymbol{U}_i^k - \frac{\Delta t}{\Delta x}(\boldsymbol{F}_{i+1/2} - \boldsymbol{F}_{i-1/2}) \tag{23}$$

where Δt is the time step; Δx the spatial step; i the spatial node index; k the time step index; q the auxiliary time step index; $\boldsymbol{U}_i^q$ the predicted solution and $\boldsymbol{F}_{i+1/2}$ the numerical flux at $x = x_{i+1/2}$. The ordinary differential equations constituted by

the source terms are solved using the third-order Runge–Kutta scheme (Gottlieb and Shu 1998)

$$\boldsymbol{U}_i^{(1)} = \boldsymbol{U}_i^q + \Delta t \boldsymbol{S}(\boldsymbol{U}_i^q) \tag{24a}$$

$$\boldsymbol{U}_i^{(2)} = \tfrac{3}{4}\boldsymbol{U}_i^q + \tfrac{1}{4}\boldsymbol{U}_i^{(1)} + \tfrac{1}{4}\Delta t \boldsymbol{S}(\boldsymbol{U}_i^{(1)}) \tag{24b}$$

$$\boldsymbol{U}_i^{k+1} = \tfrac{1}{3}\boldsymbol{U}_i^q + \tfrac{2}{3}\boldsymbol{U}_i^{(2)} + \tfrac{2}{3}\Delta t \boldsymbol{S}(\boldsymbol{U}_i^{(2)}) \tag{24c}$$

Bed evolution is computed from Eq. (6) in the same manner as Eq. (24) using the state information due to Eq. (23)

$$z_{bi}^{(1)} = z_{bi}^k + \Delta t \frac{(D-E)_i^q}{1-p} \tag{25a}$$

$$z_{bi}^{(2)} = \frac{3}{4}z_{bi}^k + \frac{1}{4}z_{bi}^{(1)} + \frac{1}{4}\Delta t \frac{(D-E)_i^{(1)}}{1-p} \tag{25b}$$

$$z_{bi}^{k+1} = \frac{1}{3}z_{bi}^k + \frac{2}{3}z_{bi}^{(2)} + \frac{2}{3}\Delta t \frac{(D-E)_i^{(2)}}{1-p} \tag{25c}$$

The spatial gradients involved in Eqs. (21c) and (22c) are discretized using a second-order central difference scheme, whilst the remaining variables are evaluated at node i.

The numerical fluxes in Eq. (23) are computed following the established TVD version of the second-order accurate WAF method (Toro 2001):

$$\boldsymbol{F}_{i+1/2} = \frac{1}{2}(\boldsymbol{F}_i + \boldsymbol{F}_{i+1}) - \frac{1}{2}\sum_{j=1}^{N} \text{sgn}(c_j) A_j \Delta \boldsymbol{F}_{i+1/2}^{(j)} \tag{26a}$$

$$\Delta \boldsymbol{F}_{i+1/2}^j = \boldsymbol{F}_{i+1/2}^{j+1} - \boldsymbol{F}_{i+1/2}^j \tag{26b}$$

where $N = 3$ is the number of conservation equations; $\Delta F_{i+1/2}^j$ the flux jump across wave j; $F_{i+1/2}^j$ the Riemann solver; $c_j = S_j \Delta x / \Delta t$ the Courant number related to wave speed S_j and A_j the WAF limiter function. Here the SUPERBEE limiter is chosen for the limiter function, as well described by Toro (2001). For the wave speeds and flux jumps involved in Eq. (26), the HLLC approximate Riemann solver is used.

The numerical algorithm described above is second-order accurate in space and time and has a linearized stability condition given by the Courant number

$$C_r = \frac{\lambda_{\max}\Delta t}{\Delta x} \le 1 \tag{27}$$

where $\lambda_{\max} = \max(u_w \pm \sqrt{gh_w}, u_s \pm \sqrt{gh_s})$.

Equation (19) for the clear-water flow layer can be solved in a similar procedure as Eq. (20), except that the HLL approximate Riemann solver is used in calculating the inter-cell fluxes (Toro 2001), instead of HLLC, because no sediment continuity equation is involved in Eq. (19).

The solution strategy for Eqs. (1)–(6), as stated above, is physically justified once the lower sediment-laden flow layer has been sufficiently developed following the dam break. At the very initial stage following the dam break, the interactions of the lower layer with the upper layer and the mobile bed may not be negligible when compared with the effects of inertia, gravity and resistance. Nevertheless, the effect of this issue on the solution strategy is diminished because the shallow water hydrodynamic theory is not rigorously applicable immediately following the dam break, as indicated by studies that resolve the detailed vertical structure of the flow (Ozmen-Cagatay and Kocaman 2010, Oertel and Bung 2012). Given this observation, the modelling studies below focus on the time after the initial period following the dam-break. The hydrodynamic time of this initial period is scaled to $t_0 = \sqrt{h_0/g}$ (h_0 = initial static water depth upstream of the dam), and thus the shallow flow theory is valid when $t \ge t_0$ (Stoker 1957). Arguably, vertical acceleration in mobile bed cases is intensified compared with fixed bed cases because the mobile bed can admit the flow vertically. In this regard, a longer initial period is expected, i.e. the shallow flow theory applies when $t \ge \beta t_0$ with $\beta > 1$.

Additionally, the governing Eqs. (9)–(12) of the SDL model are solved numerically using the same algorithm as previously proposed by Spinewine (2005a), i.e. a second-order Godunov finite-volume scheme along with the LHLL (Lateralized HLL) Riemann solver (Fraccarollo *et al.* 2003).

3 Test cases

A series of test cases is solved to verify the DL model, including comparisons with the SL (Cao *et al.* 2004) and SDL (Spinewine 2005a) models. The test cases concern flows due to instant and full dam break and progressive failure of a single and cascade landslide dams, respectively.

To quantify the difference between a numerical solution and measured data, the non-dimensional discrepancy is defined based on the L^1 norm

$$L_{st}^1 = \frac{\sum abs(\eta_i - \widehat{\eta}_i)}{\sum (h_w + h_s)_i} \tag{28a}$$

$$L_{in}^1 = \frac{\sum abs[(h_s + z_b)_i - (\widehat{h}_s + \widehat{z}_b)_i]}{\sum (h_s)_i} \tag{28b}$$

$$L_{bd}^1 = \frac{\sum abs(\Delta z_{bi} - \Delta \widehat{z}_{bi})}{\sum abs(\Delta z_{bi})} \tag{28c}$$

where L_{st}^1, L_{in}^1 and L_{bd}^1 are L^1 norms for stage, interface between the two layers and bed deformation depth, respectively. The bed deformation depth is defined by $\Delta z_{bi} = z_b - z_b(t=0)$, and $\widehat{\eta}$, $\widehat{h}_s + \widehat{z}_b$ and $\Delta \widehat{z}_b$ are measured stage, interface elevation and bed deformation, respectively, whilst C_s, $h_s + z_b$ and Δz_b are the stage, interface elevation and bed deformation from a numerical solution.

In the present work, a fixed uniform mesh is adopted, and the spatial step is sufficiently fine to ensure mesh independence of the solution, i.e. essentially equivalent solutions are obtained with an even finer mesh. The spatial step Δx is set to be 0.02 m and

the Courant number C_r is 0.5. Bed porosity $p = 0.4$ is adopted for all the test cases.

3.1 Instant and full dam break (test case 1)

Mobile bed dam-break experiments were carried out in a flume at the Université Catholique de Louvain, Belgium (Spinewine 2005a). The flume was 6 m long, 0.25 m wide and 0.70 m high. Dam break was simulated by the rapid downward removal of a thin gate at the middle of the flume. The experiments were conducted over an initially horizontal bed composed of non-cohesive sediments, saturated with water and extending on both sides of the idealized "dam" represented by the gate. Here, one experimental case is revisited, with an initial water depth $h_0 = 35$ cm upstream the dam. The medium diameter of the bed material composed of PVC (Polyvinylchloride) pellets was 3.92 mm and the density was 1580 kg m^{-3}. Numerical modelling was performed within the time period before the forward and backward waves reached the downstream and upstream boundaries, where the boundary conditions can be simply set at the initial static status. For the SDL model, the sediment concentration C_s in

the lower layer is set to be 0.22 following Spinewine (2005a), except otherwise specified. The bed roughness n_b is set to be 0.026 m$^{-1/3}$ s following Zech *et al.* (2008). The modification coefficient ϕ adopted in the DL and SL models and the interface roughness n_w are determined by fitting to the measured stage. It is found that $\phi = 2.0$ for the DL model, $\phi = 3.0$ for the SL model and $n_w = 0.006$ m$^{-1/3}$ s for the DL and SDL models lead to satisfactory agreement with the measured data.

Figure 2 shows the water surface and bed profiles measured and computed by the DL, SDL and SL models. The bed scour depth and flood wave fronts are reproduced well by the three models. Figure 3 illustrates the water surface and bed profiles along with the interface computed from the DL and SDL models. Undesirable non-physical oscillations of the water surface profiles and interfaces from the SDL model are spotted (Fig. 3b). Quantitatively, the values of the L^1 norms of the DL, SDL and SL models for this case are similar (Table 1). The temporal and spatial scales of the flow, sediment transport and bed evolution in this particular case are so small that the performances of the three models are hardly distinguishable (Table 1), except the oscillations due to the SDL model in Fig. 3b.
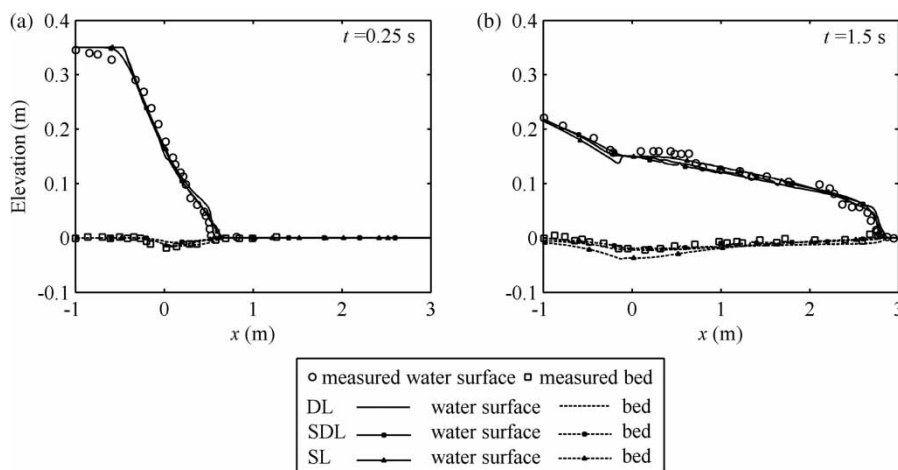

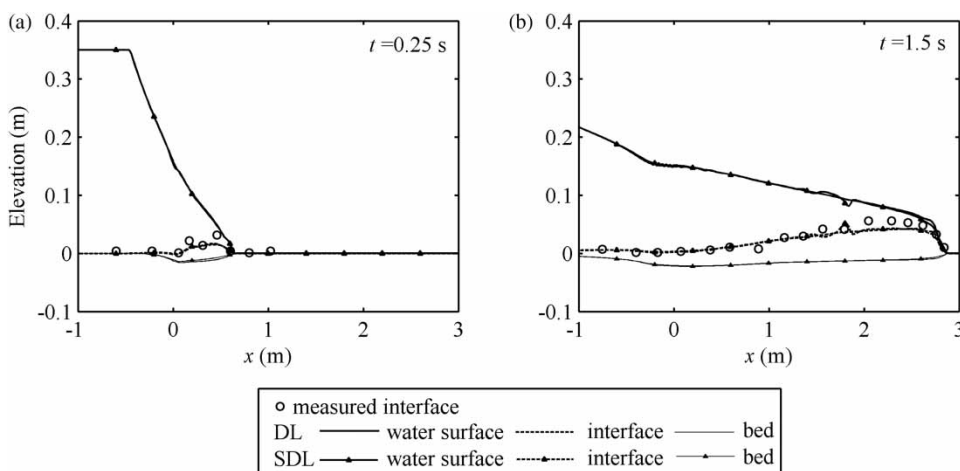Figure 2   Computed water surface and bed profiles compared with measured data

Figure 3   Water surface and bed profiles along with the interface from the DL and SDL models

Table 1 L^1 norm of the DL, SDL and SL models for instant and full dam break (test case 1)

Time	$t = 0.25$ s			$t = 1.5$ s		
L^1	DL (%)	SDL (%)	SL (%)	DL (%)	SDL (%)	SL (%)
L^1_{st}	2.68	2.75	2.71	3.72	3.93	3.89
L^1_{in}	3.12	3.11	n/a	3.46	3.52	n/a
L^1_{bd}	4.45	4.78	3.89	4.47	4.84	5.22

3.2 Progressive failure of a single and cascade landslide dams (test cases 2 and 3)

This subsection focuses on the flows due to progressive failure of a single and cascade landslide dams, in contrast to the instant and full dam break (test case 1) revisited above. A series of flume experiments on landslide dam breach and the resulting floods is documented by Cao *et al.* (2011a, 2011b). These experiments were carried out in a flume of dimensions $80 \times 1.2 \times 0.8$ m (Fig. 4) and bed slope 0.001. A set of 12 automatic water-level probes was used to measure the stage hydrographs at 12 cross-sections along the flume. In the experiments, the dams failed by virtue of erosion of the overtopping flow when there was no initial breach. The experiments provided a unique and systematic set of observed data for testing mathematical models of dam breach and the resulting floods.

To demonstrate the performance of the models, two experimental runs are revisited, i.e. F-Case 11 and T-Case 2 without initial dam breach (Cao *et al.* 2011a, 2011b). In both cases, the initial upstream and downstream slopes of the dam were 1/2 and 1/3, respectively. The medium diameter of the non-cohesive dam material was 0.8 mm and the specific gravity of the sediment was 1.65. For F-Case 11, the single dam was initially 0.4 m high, located at about 41 m from the inlet of the flume. The inlet flow discharge was 0.042 m³ s⁻¹. The initial static water depths immediately upstream and downstream of the dam were 0.054 m and 0.048 m, respectively. For T-Case 2 that involved two dams in cascade, both dams were 0.4 m high initially, and located at 41 m and 60.3 m, respectively, from the inlet of the flume. The inlet discharge was 0.025 m³ s⁻¹. The initial static water depth was 0.054 m immediately upstream the first dam, whilst it was 0.048 m immediately upstream and downstream the second dam. At the inlet boundary, flow discharge was specified, and the water depth and velocity were determined by the method of characteristics. There was no sediment-laden flow layer at the inlet. Besides, a 0.15-m high-weir was set at the flume outlet. Observation during the course of the experiments showed that a hydraulic drop occurred downstream of the weir, so the outflow did not affect the flow upstream of the weir. Here, a transmissive condition (Toro 2001) was imposed at the downstream boundary (80 m), and all the primitive variables in the outlet nodes were equal to those of internal nodes closest to the boundary.

For this modelling exercise, a bed roughness $n_b = 0.012$ m⁻¹ᐟ³ s is used for all the three models. The modification coefficient ϕ for the DL and SL models, the interface roughness n_w for the DL and SDL models as well as the lower layer sediment concentration C_s in the SDL model are first calibrated using the measured stage hydrographs from the experiments for a single dam failure F-Case 11, and then directly applied for T-Case 2 of cascade dam failure. It is found that the modification coefficient $\phi = 4.5$ for the DL model, $\phi = 6.0$ for the SL model, interface roughness $n_w = 0.006$ m⁻¹ᐟ³ s for the DL and SDL models and the sediment concentration $C_s = 0.1$ for the SDL model lead to the best agreements with the measured data.

Figures 5 and 6 show the computed stage hydrographs by the DL, SDL and SL models, and the measured data at selected cross-sections in both cases. For F-Case 11, CS5 and CS12 are located upstream and downstream the dam, respectively. For T-Case 2, CS1 and CS5 are upstream the first dam, CS8 is between the two dams and CS12 is downstream the second dam. The cross-sections CS1, CS5, CS8 and CS12 are located at 19 m, 40 m, 54 m and 73.5 m, respectively, from the inlet of the flume (Fig. 4). It is seen from Figs. 5 and 6 that the computed stages by the three models are in fairly good agreement with the measured data.

Figures 7 and 8 illustrate the water surface and bed profiles computed from the DL, SDL and SL models, along with the measured data for the water surface elevation and the interface from the DL and SDL models. In fact, the progressive failure of the dams is explicitly represented by the evolution of the bed profile. Regardless of the fact that the stage hydrographs at selected cross-sections by the SDL model match the measured data fairly well (Figs. 5 and 6), the computed bed and
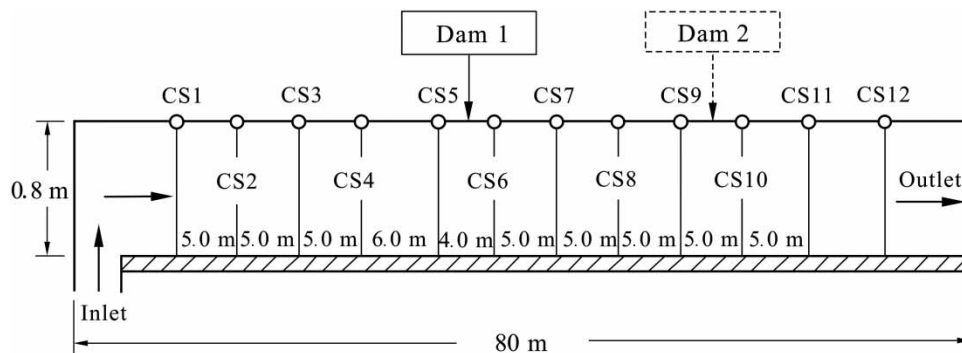

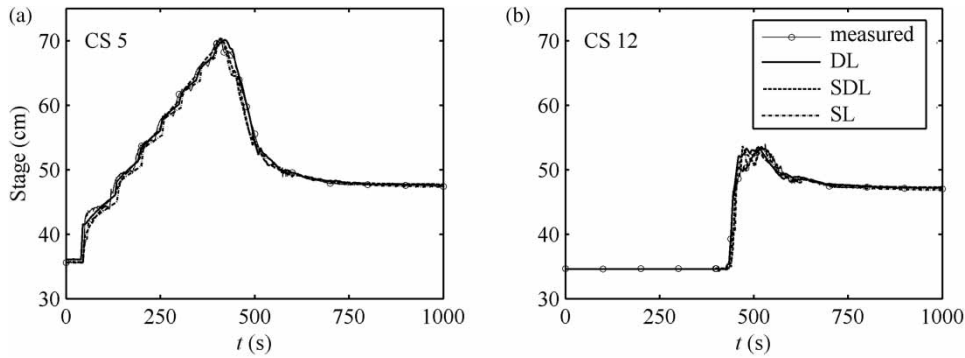Figure 4 Experimental setup for landslide dam failure

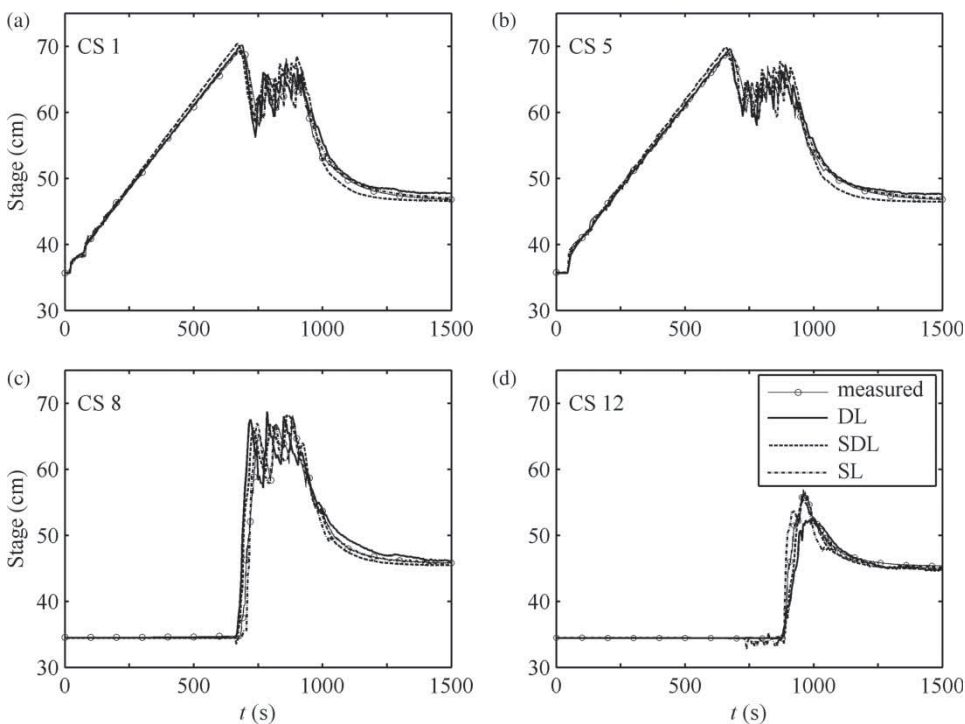Figure 5   Stage hydrographs for a single landslide dam breach

Figure 6   Stage hydrographs for cascade landslide dam breach

water surface profiles by the SDL model exhibit serious numerical oscillations and deviate from the measured data significantly in some locations (Figs. 7a2–d2 and 8a2–e2). Obviously, the numerical results from the SDL model are badly spoiled, rendering the sediment-laden flow layer hardly recognizable when compared against the results from the DL model (Figs. 7a1–d1 and 8a1–e1). It is critical to point out that the numerical oscillations are inherent to the SDL model, as the use of a reduced or increased Courant number (e.g. $C_r = 0.1, 0.9$) does not eliminate the oscillations (not shown). Yet, it is premature to conclude if the numerical oscillations result from the assumption of constant sediment concentration embedded in the SDL model or the loss of hyperbolicity, as the Froude number is found to exceed 1.0 locally (not shown). Indeed, immediately following the onset of the dam breach (e.g. 410 s in Fig. 7 and 675 s in Fig. 8), the SDL model's

performance is comparable to the DL and SL models when compared with the measured water surface elevation. However, at other instants when the flow is rapidly varied longitudinally and clearly exhibits complex structure such as subcritical-to-supercritical transitions and hydraulic jumps (e.g. 430 s and 450 s in Fig. 7 and 700 s and 900 s in Fig. 8), the SDL model performs poorly when compared with the measured data, in sharp contrast to the DL and SL models. Comparatively, the DL model performs appreciably better than the traditional SL model in resolving the complex flow structures (hydraulic jumps) as shown in Figs. 7 and 8.

Echoing Figs. 7 and 8, the values of the L_{st}^1 (Tables 2 and 3) provide further testament for the improved performance of the DL model over the SDL and SL models in comparison with measured data. Specifically, the DL and SDL models feature,

Figure 7   Water surface, interface and bed profiles for a single landslide dam failure. DL: left; SDL: middle; SL: right

respectively, the minimum and maximum L_{st}^1 values, whilst the SL model lies in between the two, consistently through time. Particularly, when the flow is rapidly varied (e.g. 430 s in Fig. 7 and 700 s in Fig. 8), the L_{st}^1 values of the SDL model are twice or even greater than those of the DL model (Tables 2 and 3). These observations lead one to comment, if only briefly, that the DL model is physically enhanced over the SL and SDL models and therefore performs the best, though the computational cost is appreciably increased by approximately 40 and 8% as compared with SL and SDL models, respectively.

The whole processes of the dam failure, flow, sediment transport and bed evolution resolved by the DL model can be briefly
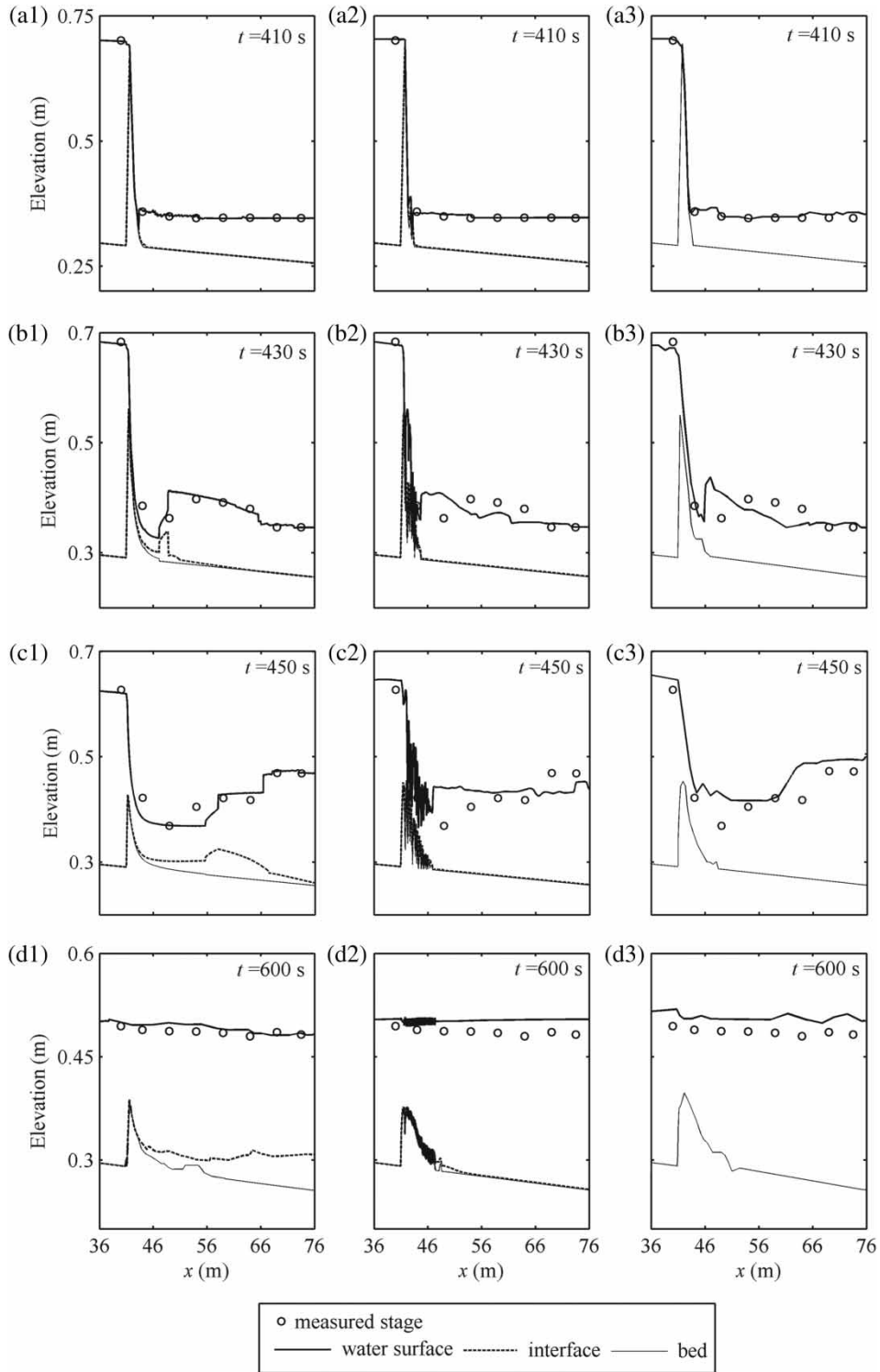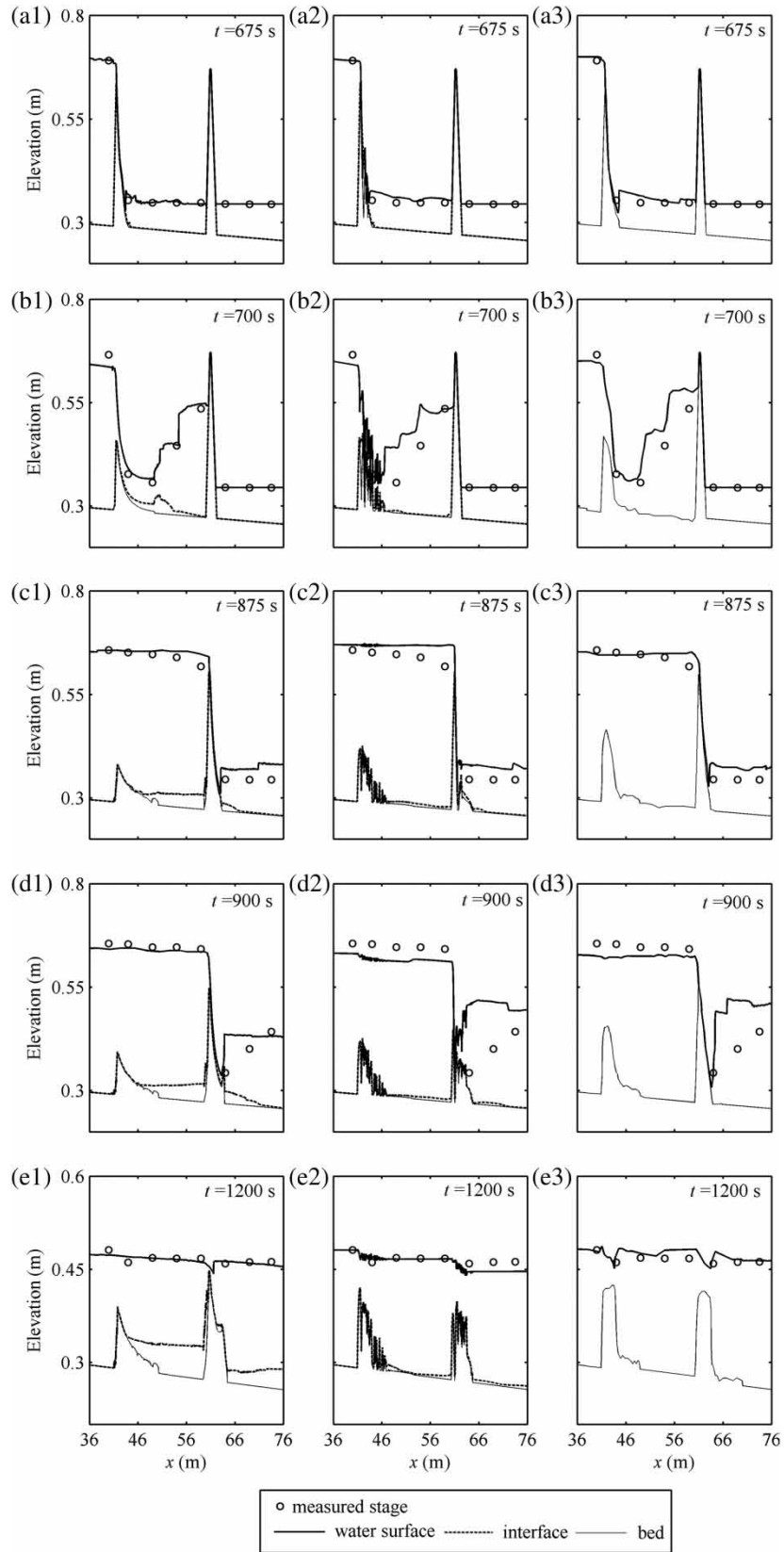
Figure 8   Water surface, interface and bed profiles for cascade landslide dam failure. DL: left; SDL: middle; SL: right

Table 2 L_{st}^1 of DL, SDL and SL models for a single landslide dam failure (test case 2)

Time	$t = 410$ s	$t = 430$ s	$t = 450$ s	$t = 600$ s	Average
DL (%)	0.12	6.52	8.54	4.43	4.90
SDL (%)	0.13	13.89	16.35	6.85	9.31
SL (%)	0.13	8.53	11.45	6.45	6.64

interpreted. For F-Case 11, at $t = 410$ s, the water flows over the top of the dam and starts to erode the toe (Fig. 7a1). At $t = 430$ s, the overtopping flow erodes the downstream surface of the dam, causing the formation of the sediment-laden flow layer (Fig. 7b1), and a hydraulic jump is formed around the dam site, which is characterized by the variation of Froude number (not shown). Compared with that at $t = 430$ s, the dam is further eroded at $t = 450$ s (Fig. 7c1), and the sediment-laden flow layer develops more fully. At this stage, two hydraulic jumps exist downstream of the dam. After $t > 600$ s, the free surface of the flow is nearly horizontal, unable to further erode the dam, and the dam failure process essentially terminates (Fig. 7d1). For T-Case 2, at $t = 675$ s, the water flows over the first dam, and the toe starts to be eroded (Fig. 8a1). At $t = 700$ s, the overtopping flow further erodes the first dam, the sediment-laden flow layer forms, and two hydraulic jumps occur between the two dams (Fig. 8b1). At $t = 875$ s (Fig. 8c1), the erosion of the first dam increases and the sediment-laden flow layer between the two dams develops further. Additionally, the overtopping flow starts to erode the downstream surface of the second dam and thus the sediment-laden flow layer forms downstream. At $t = 900$ s, the second dam is further eroded, leading to the amplification of the sediment-laden flow layer downstream, whilst a hydraulic jump is also formed around the second dam site (Fig. 8d1). After $t > 1200$ s, the water surface tends to be rather smooth and the dam failure process almost terminates. Clearly, the second dam is not eroded as fully as the first dam (Fig. 8e1).

Overall, the SL model performs well compared with the measured water surface elevation, as previously stated in regard to its extended version (Cao *et al.* 2011a, 2011c). The DL model shows promise for successful modelling of the highly unsteady and complex flows due to progressive failure of landslide dams, either in a single setting or in a cascade. It resolves the physical phenomenon in a more detailed manner, facilitating a resolution of the sediment-laden flow layer, which is unavailable from the SL model. The SDL model performs poorly compared with the measured data. Theoretically, the latter fact arises from the

assumption of constant sediment concentration in the lower layer, which essentially breaks the fundamental mass conservation law for sediment.

3.3 *Progressive failure of a dike (test case 4)*

This subsection aims to evaluate the three models' ability to reproduce the morphological evolution of a breaching dike. An experimental test (Test-18) is revisited, which was carried out by Schmocker and Hager (2012) in a flume that is 8 m long, 0.4 m wide and 0.70 m high. In this case, the initial single dike was 0.2 m high, 0.2 m wide and located at about 1.0 m from the inlet of the flume. The initial upstream and downstream slopes of the dike were both 1 : 2. The medium diameter of the non-cohesive dike material was 2.0 mm and the specific gravity of the sediment was 1.65. The inlet unit-width discharge was $0.08 \, \mathrm{m^2 \, s^{-1}}$. The initial water depths immediately upstream and downstream of the dike were 0.2 m and 0.0 m, respectively. At the inlet boundary, flow discharge was specified, and the water depth and velocity were determined by the method of characteristics. A free flow was imposed at the channel end as the downstream boundary condition, following Pontillo *et al.* (2010) for similar test cases using the two-phase model developed by Greco *et al.* (2008).

For the SDL model, the sediment concentration C_s of the sediment-laden layer is assumed to be 0.1. The modification coefficients ϕ adopted in the DL and SL models are both 6.0. The interface roughness n_w adopted in the DL and SDL models is set to be $0.006 \, \mathrm{m^{-1/3} \, s}$. For the three models, bed roughness n_b is $0.015 \, \mathrm{m^{-1/3} \, s}$.

Figure 9 shows the water surface and bed profiles from the DL, SDL and SL models, along with the measured bed elevation and interface computed from the DL and SDL models. Overall, both the DL and SL models can reasonably reproduce the breaching process of the dike. As seen from Fig. 9, the DL model performs the best, followed by the SL model, and the SDL model performs the worst due to the serious non-physical oscillations. This observation is corroborated quantitatively by the values of L_{bd}^1 (Table 4). The average L_{bd}^1 of the DL, SDL and SL models are 10.63, 13.83 and 10.94%, respectively. Obviously, the maximum error is due to the SDL model. Pontillo *et al.* (2010) modelled similar but different experimental cases, and the root-mean-square error, instead of the L^1 norm, was used to measure the discrepancies between computational results and measured data. Therefore, a comparison of the performances of the DL and two-phase models is not strictly justified. Nevertheless, the agreement of the DL and SL models with the measured

Table 3 L_{st}^1 of DL, SDL and SL models for cascade landslide dam failure (test case 3)

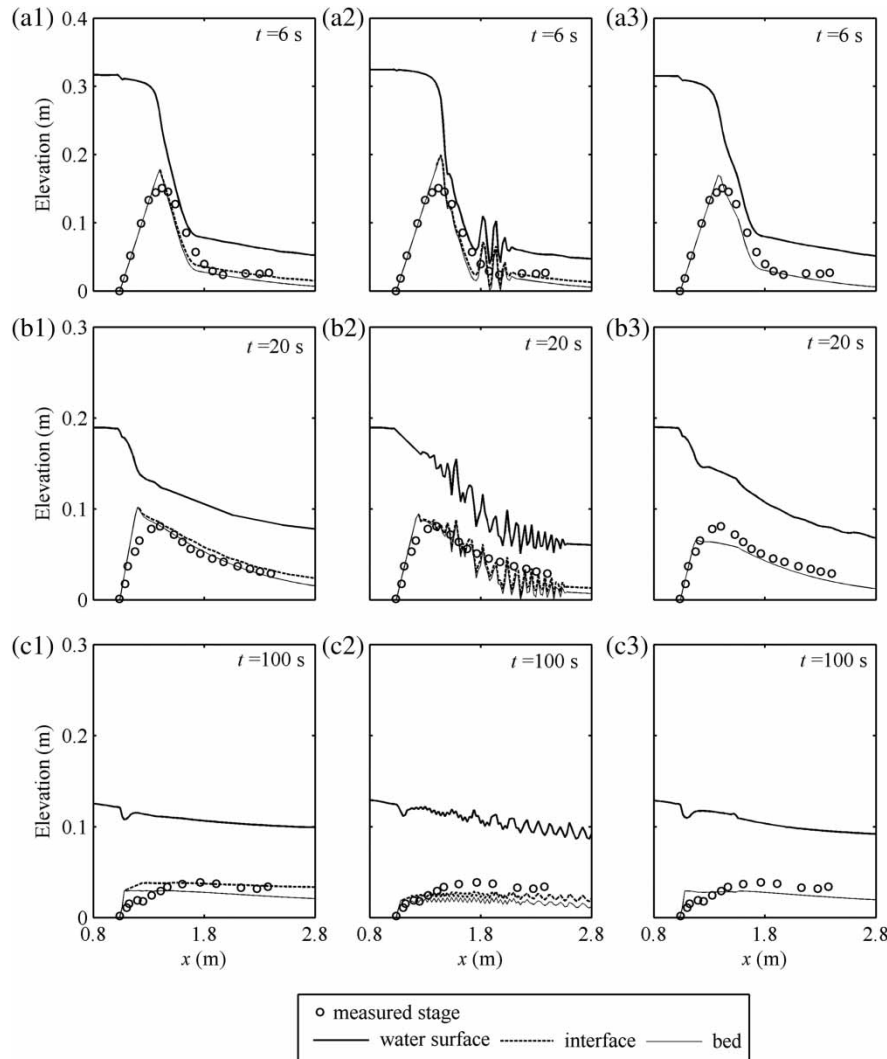| Time	$t = 675$ s	$t = 700$ s	$t = 875$ s	$t = 900$ s	$t = 1200$ s	Average
DL (%)	0.9	4.26	8.19	11.18	3.72	5.65
SDL (%)	1.52	13.48	11.45	16.68	4.05	9.44
SL (%)	1.02	5.24	9.06	14.84	3.89	6.81

Figure 9   Water surface, interface and bed profiles for a dike breach. DL: left; SDL: middle; SL: right

Table 4 L_{bd}^1 of DL, SDL and SL models for test case 4

Time	$t = 6$ s	$t = 20$ s	$t = 100$ s	Average
DL (%)	13.64	9.94	8.36	10.64
SDL (%)	17.52	11.42	12.56	13.83
SL (%)	12.67	10.15	9.89	10.90

bed profile (Fig. 9) is approximately equivalent to or apprecia-bly better than its counterpart shown in Pontillo *et al.* (2010, Figs. 2–5), which was claimed to be an improvement over the traditional De Saint-Venant–Exner model.

4   Discussion

4.1   *Sensitivity analysis*

Numerical tests are conducted to evaluate the sensitivity of the computational results to model parameters. In general, the results

with tuned parameters are qualitatively similar to those shown in Figs. 2, 3 and 5–9 when compared with the measured data.

Specifically, for test case 1, the sediment concentration C_s of the lower layer in the SDL model is tuned by about 22% of the calibrated value (i.e. $C_s = 0.22 \pm 0.5$). Shown in Fig. 10 are the water surface and bed profiles along with the interface computed from the SDL model, corresponding to different sed-iment concentrations presumed for the lower sediment-laden flow layer. In Table 5 the corresponding L^1 values are pro-vided. From Fig. 10, it is found that the computational results of the SDL model are very sensitive to the presumed value of C_s. This is apparently echoed by the L^1 values (Table 5). Com-paratively, L_{in}^1 is most sensitive to C_s, whilst L_{st}^1 and L_{bd}^1 are less sensitive. At $t = 1.5$ s, L_{in}^1 is nearly doubled in response to a variation of C_s by 22% (Table 5). It is also shown in Table 5 that the sensitivity of the L^1 values to C_s would increase with time.

Likewise, the modification coefficient ϕ in the DL model is tuned by 50% of its calibrated value (i.e. $\phi = 2.0 \pm 1.0$), and the
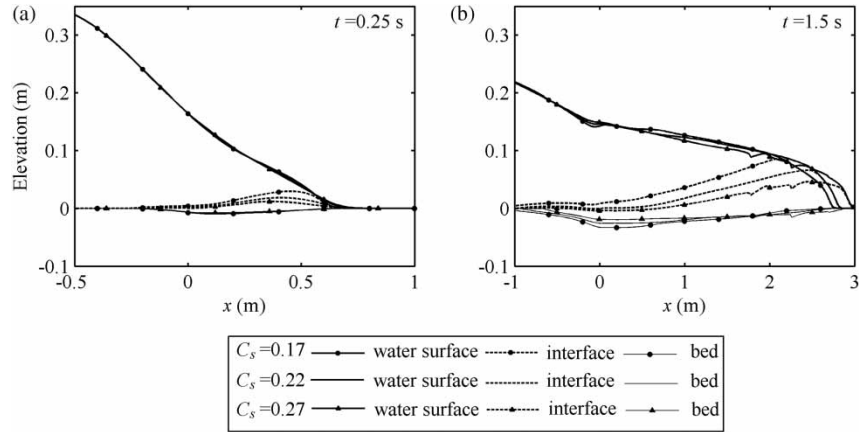
Figure 10   Water surface and bed profiles along with interface from the SDL model assuming different sediment concentrations

Table 5 L^1 norm of SDL model with different C_s for test case 1

| L^1 | C_s | L^1 norm | |
		$t = 0.25$ s	$t = 1.5$ s
L^1_{st}	0.17	2.88%	6.19%
	0.22	2.75%	3.93%
	0.27	3.02%	5.97%
L^1_{in}	0.17	4.45%	7.16%
	0.22	3.11%	3.52%
	0.27	4.47%	7.09%
L^1_{bd}	0.17	5.01%	7.74%
	0.22	4.92%	5.04%
	0.27	5.49%	7.88%

Table 6 L^1 norm of DL model with different ϕ for test case 1

| L^1 | ϕ | L^1 norm | |
		$t = 0.25$ s	$t = 1.5$ s
L^1_{st}	1.0	2.71%	4.13%
	2.0	2.68%	3.72%
	3.0	2.73%	3.91%
L^1_{in}	1.0	3.27%	4.34%
	2.0	3.12%	3.46%
	3.0	3.18%	4.15%
L^1_{bd}	1.0	6.33%	6.21%
	2.0	4.45%	4.47%
	3.0	5.89%	5.64%

results are shown in Fig. 11 and Table 6. Indeed, the results are appreciably sensitive to the tuned parameter ϕ. As seen from Fig. 11, the bed deformation seems to be more sensitive to the value of ϕ than the stage and interface, which is supported by the L^1 values in Table 6. This is in contrast to the observation that the interface profile is most sensitive to C_s in the SDL model (Fig. 10 and Table 5). Physically, this is determined by the fact that ϕ is directly embedded in the relationships for sediment entrainment in the DL model, i.e. Eqs. (17) and (18), and therefore in the

bed deformation (Eq. 6), whereas C_s is explicitly involved in the equations of the two layers in the SDL model, i.e. Eqs. (9)–(12), instead of the bed evolution (Eq. 7). Most notably, the sensitivity to ϕ in the DL model is considerably constrained compared with that to C_s in the SDL model. This is substantiated by the fact that the increase of L^1_{st}, L^1_{in} and L^1_{bd} of the DL model in response to the change of ϕ (by 50%) is considerably smaller than its counterpart of the SDL model in connection with the change of C_s (by 22%) (see Tables 5 and 6). Consequently, the computational results
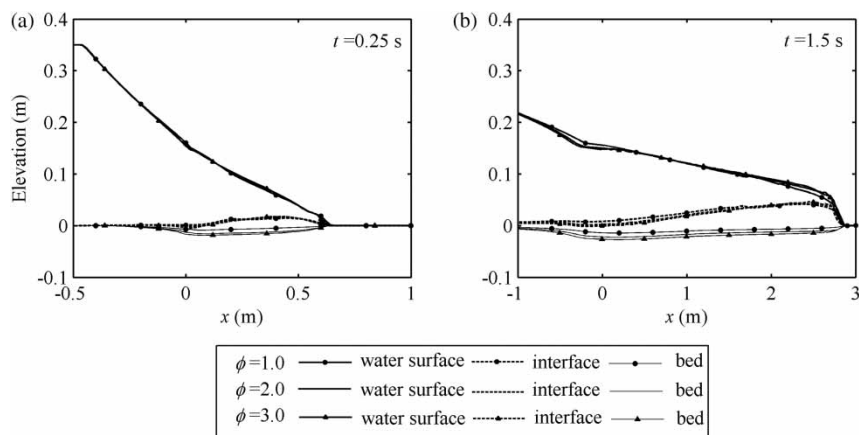

Figure 11   Water surface and bed profiles along with interface from the DL model assuming different modification coefficient ϕ

Table 7 L_{st}^1 of DL model with different ϕ for test case 2

ϕ	$t = 410$ s	$t = 430$ s	$t = 450$ s	$t = 600$ s	Average
3.0	0.15%	9.32%	11.27%	7.11%	6.96%
4.5	0.12%	6.52%	8.54%	4.43%	4.90%
6.0	4.43%	8.83%	8.56%	4.52%	6.59%

Table 8 L_{st}^1 of DL model with different ϕ for test case 3

ϕ	$t = 675$ s	$t = 700$ s	$t = 875$ s	$t = 900$ s	$t = 1200$ s	Average
3.0	1.05%	6.22%	11.88%	13.28%	4.68%	7.42%
4.5	0.9%	4.26%	8.19%	11.18%	3.72%	5.65%
6.0	4.54%	6.67%	11.06%	12.09%	3.83%	7.66%

Table 9 L_{bd}^1 of DL model with different ϕ for test case 4

ϕ	$t = 6$ s	$t = 20$ s	$t = 100$ s	Average
4.0	18.62%	13.56%	9.69%	13.96%
6.0	13.64%	9.94%	8.36%	10.64%
8.0	17.69%	14.27%	10.83%	14.26%

are more sensitive to the presumed sediment concentration C_s in the SDL model than to the modification coefficient ϕ in the DL model, which characterizes a major limitation of the SDL model.

For test cases 2, 3 and 4, numerical experiments are carried out to ascertain the sensitivity of the computational results of the DL model to the parameter ϕ. Generally, the stage, interface and bed deformation (not shown) in line with tuned parameter ϕ are similar to those illustrated in Figs. 2, 3 and 5–9 qualitatively. However, the L^1 values increase to a certain extent, as shown in Tables 7–9. Typically, as the modification coefficient ϕ of the DL model is tuned by one-third of the calibrated values for test cases 2, 3 and 4, the average values of L_{st}^1 for test cases 2 and 3 and of L_{bd}^1 for test case 4 increase by approximately 30–40%.

4.2   *Variation of sediment concentration*

Theoretically, both the DL and SL models are built upon the fundamental mass conservation law for sediment, so they can reflect the variation of sediment concentration in space and time. To illustrate this, the sediment concentration profiles from the DL, SDL and SL models for the instant and full dam-break case (test case 1) are shown in Fig. 12. Here, for the DL and SDL models, the averaged sediment concentration over the whole flow depth is defined as $C_h = C_s h_s / (h_w + h_s)$. According to the DL model, at 0.25 s following the dam-break, the sediment concentration C_s in the lower layer has attained a rather high value of approximately 0.3, and at 1.5 s it is characterized by spatial expansion and also considerable decrease except around the forefront of the flood wave. It is apparent that C_s varies substantially in space and time, as resolved by the DL model. Hence, the assumption of a constant sediment concentration C_s in the lower layer is not justified. The qualitative similarity of the longitudinal profiles of the whole depth-averaged sediment concentration C_h from the SDL model to those due to the DL model does not justify the SDL model because it is the C_s, rather than C_h, that is directly embedded in the SDL model.

5   Conclusions

A physically enhanced DL model is developed for dam-break flows over mobile bed. It is new as sediment mass conservation is explicitly incorporated in lieu of the assumption of constant sediment concentration generic to existing DL models. The numerical algorithm proposed for the new model is effective and satisfactorily accurate. The new model is tested against laboratory experimental data of typical dam-break flows due to instant and full dam break and progressive failure of a dike and landslide dams, either in a single setting or in cascade. Enhanced performance of the new model is demonstrated over a SDL model and a SL model. Extension of the present DL model to two dimensions is warranted for field cases with complex and irregular topography. It should find wide applications in modelling sharply stratified dam-break flows over mobile bed.
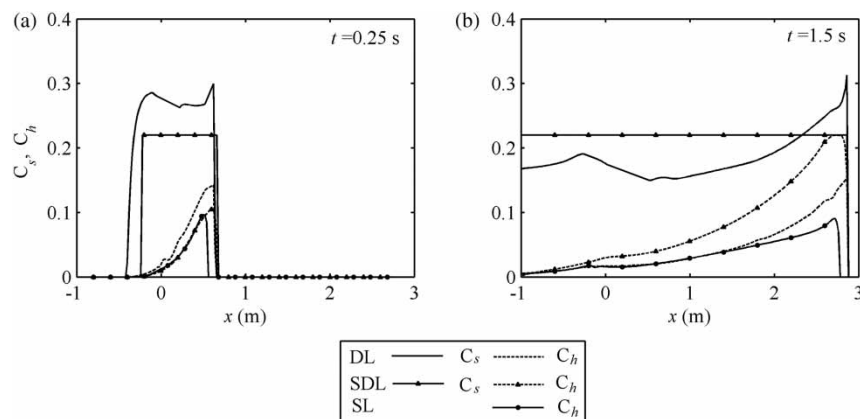

Figure 12   Sediment concentration profiles from the DL, SDL and SL models

Notation

C_b	=	volumetric sediment concentration of the bed (−)
C_h	=	volumetric sediment concentration over the whole water depth (−)
C_r	=	Courant number (−)
C_s	=	volumetric sediment concentration of sediment-laden flow layer (−)
c_e	=	bedload sediment transport capacity (−)
d	=	medium sediment particle diameter (m)
E	=	vector defined in Eq. (21)
E, D	=	sediment entrainment and deposition fluxes, respectively (m s^{-1})
E_w	=	mass exchange flux of clear water between the upper and lower layers (m s^{-1})
e_b	=	bed erosion rate (m s^{-1})
e_w	=	coefficient for mass exchange of clear water (−)
F	=	vector defined in Eq. (22)
g	=	gravitational acceleration (m s^{-2})
h_s	=	depth of sediment-laden flow layer (m)
h_w	=	depth of clear-water flow layer (m)
i	=	index denoting the spatial node
k	=	index denoting the time step
L^1	=	norm to measure error (−)
L^1_{st}, L^1_{in} and L^1_{bd}	=	norms for stage, interface and bed deformation depth, respectively.
m	=	exponent (−)
n_b	=	bed roughness (m$^{-1/3}$ s)
n_w	=	interface roughness (m$^{-1/3}$ s)
p	=	bed sediment porosity (−)
q	=	index denoting the auxiliary time step
q_b	=	unit-width bedload transport rate at transport capacity status (m^2 s^{-1})
R	=	source term for clear-water flow layer
R_p	=	particle Reynolds number (−)
Ri	=	Richardson number (−)
s	=	specific gravity of sediment (−)
S	=	source term for sediment-laden flow layer
U	=	vector of conserved variables of sediment-laden flow layer
u_s	=	mean velocity of sediment-laden flow layer (m s^{-1})
u_w	=	mean velocity of clear-water flow layer (m s^{-1})
u_*	=	friction velocity (m s^{-1})
x	=	streamwise coordinate (m)
T	=	vector of conserved variables of clear-water flow layer
t	=	time (s)
z_b	=	bed elevation (m)
Δx	=	spatial step in the x direction (m)
Δt	=	time step (s)
Δz_b	=	bed deformation depth (m)
η	=	stage (m)
ν	=	kinematic viscosity of water (m^2 s^{-1})
θ	=	Shields parameter (−)
θ_c	=	threshold Shields parameter for initiation of sediment movement (−)
λ_{max}	=	maximum celerity (m s^{-1})
ρ_w and ρ_s	=	densities of water and sediment, respectively (kg m^{-3})
ρ_c and ρ_0	=	densities of water–sediment mixture and saturated bed (kg m^{-3})
τ_b	=	bed shear stress (kg m^{-1} s^{-2})
τ_w	=	interface shear stress (kg m^{-1} s^{-2})
ϕ	=	modification coefficient (−)
ω	=	settling velocity of a single sediment particle in tranquil clear water (m s^{-1})

References

Batchelor, G.K. (1967). *An introduction to fluid dynamics*. Cambridge University Press, Cambridge.

Cao, Z., Carling, P. (2002). Mathematical modelling of alluvial rivers: Reality and myth. Part II: Special issues. *Proc. Inst. Civil Eng. Water Maritime Eng.* 154(4), 297–307.

Cao, Z., Pender, G., Wallis, S., Carling, P. (2004). Computational dam-break hydraulics over erodible sediment bed. *J. Hydraulic Eng.* 130(7), 689–703.

Cao, Z., Yue, Z., Pender, G. (2011a). Flood hydraulics due to cascade landslide dam failure. *J. Flood Risk Manage.* 4(2), 104–114.

Cao, Z., Yue, Z., Pender, G. (2011b). Landslide dam failure and flood hydraulics. Part I: Experimental investigation. *Nat. Hazards* 59(2), 1003–1019.

Cao, Z., Yue, Z., Pender, G. (2011c). Landslide dam failure and flood hydraulics. Part II: Coupled mathematical modelling. *Nat. Hazards* 59(2), 1021–1045.

Capart, H., Young, D. (1998). Formation of a jump by the dam-break wave over a granular bed. *J. Fluid Mech.* 372, 165–187.

Capart, H., Young, D. (2002). Two-layer shallow water computations of torrential geomorphic flows. Proc. Int. Conf. *River flow*, Louvain-la-Neuve, 1003–1012, D. Bousmar, Y. Zech, eds. Balkema, Rotterdam NL.

Castro, M., Frings, J., Noelle, S., Pares, C., Puppo, G. (2010). On the hyperbolicity of two- and three-layer shallow water equations. Proc. Int. Conf. *Hyperbolic Problems*, Beijing, 657–664, T. Li, S. Jiang, eds. Higher Education Press, Beijing.

Chen, S.C., Peng, S.H. (2006). Two-dimensional numerical model of two-layer shallow water equations for confluence simulation. *Adv. Water Res.* 29(11), 1608–1617.

Chien, N., Wan, Z.H. (1999). *Mechanics of sediment transport*. ASCE Press, New York.

Fraccarollo, L., Capart, H. (2002). Riemann wave description of erosional dam-break flows. *J. Fluid Mech.* 461, 183–228.

Fraccarollo, L., Capart, H., Zech, Y. (2003). A Godunov method for the computation of erosional shallow water transients. *Int. J. Numer. Meth. Fluids* 41(9), 951–976.

Gottlieb, S., Shu, C.W. (1998). Total variation diminishing Runge–Kutta schemes. *Math. Comput.* 67, 73–85.

Goutière, L., Soares-Frazão, S., Zech, Y. (2011). Dam-break flow on mobile bed in abruptly widening channel: Experimental data. *J. Hydraulic Res*. 49(3), 367–371.

Greco, M., Iervolino, M., Leopardi, A. (2008). Two-phase depth-integrated model for unsteady river flow. Proc. Int. Conf. *Hydro-science and engineering*, Nagoya, 1126–1135, S. Wang, ed. Nagoya University Press, Nagoya.

Greco, M., Iervolino, M., Leopardi, A., Vacca, A. (2012). A two-phase model for fast geomorphic shallow flows. *Int. J. Sediment Res.* 27(4), 409–425.

Kim, J., LeVeque, R.J. (2008). Two-layer shallow water system and its applications. Proc. Int. Conf. *Hyperbolic problems*, Maryland, 737–743, E. Tadmor, J.G. Liu, A.E. Tzavaras, eds. AMS Press, Providence RI.

La Rocca, M., Adduce, C., Sciortino, G., Pinzon, A.B., Boniforti, M.A. (2012). A two-layer shallow-water model for 3D gravity currents. *J. Hydraulic Res.* 50(2), 208–217.

Leal, J.G.A.B., Ferreira, R.M.L., Cardoso, A.H. (2006). Dam-break wave-front celerity. *J. Hydraulic Eng.* 132(1), 69–76.

Leal, J.G.A.B., Ferreira, R.M.L., Cardoso, A.H. (2010a). Geomorphic dam-break flows. Part I: Conceptual model. *Proc. Inst. Civil Eng. Water Manage.* 163(6), 297–304.

Leal, J.G.A.B., Ferreira, R.M.L., Cardoso, A.H. (2010b). Geomorphic dam-break flows. Part II: Numerical simulation. *Proc. Inst. Civil Eng. Water Manage.* 163(6), 305–313.

LeVeque, R.J. (2002). *Finite volume methods for hyperbolic problems*. Cambridge University Press, Cambridge.

Meyer-Peter, E., Müller, R. (1948). Formulas for bed-load transport. Proc. 2nd *IAHR Congress* Stockholm Appendix 2, 39–64.

Oertel, M., Bung, D.B. (2012). Initial stage of two-dimensional dam-break waves: Laboratory versus VOF. *J. Hydraulic Res.* 50(1), 89–97.

Ozmen-Cagatay, H., Kocaman, S. (2010). Dam-break flows during initial stage using SWE and RANS approaches. *J. Hydraulic Res.* 48(5), 603–611.

Parker, G., Fukushima, Y., Pantin, H.M. (1987). Experiments on turbidity currents on an erodible bed. *J. Hydraulic Res.* 25(1), 123–147.

Pontillo, M., Schmocker, L., Greco, M., Hager, W.H. (2010). 1D numerical evaluation of dike erosion due to overtopping. *J. Hydraulic Res.* 48(5), 573–582.

Richardson, J., Zaki, W. (1954). Sedimentation and fluidisation: Part 1. *Trans. Inst. Chem. Eng.* 32, 35–53.

Savary, C., Zech, Y. (2007). Boundary conditions in a two-layer geomorphological model: Application to a hydraulic jump over a mobile bed. *J. Hydraulic Res.* 45(3), 316–332.

Schmocker, L., Hager, W.H. (2012). Plane dike-breach due to overtopping: Effects of sediment, dike height and discharge. *J. Hydraulic Res.* 50(6), 576–586.

Soares-Frazão, S., Canelas, R., Cao, Z., Cea, L., Chaudhry, H.M., Die Moran, A., El Kadi, K., Ferreira, R., Cadórniga, I.F., Gonzalez-Ramirez, N., Greco, M., Huang, W., Imran, J., Le Coz, J., Marsooli, R., Paquier, A., Pender, G., Pontillo, M., Puertas, J., Spinewine, B., Swartenbroekx, C., Tsubaki, R., Villaret, C., Wu, W., Yue, Z., Zech, Y. (2012). Dam-break flows over mobile beds: Experiments and benchmark tests for numerical models. *J. Hydraulic Res.* 50(4), 364–375.

Spinewine, B. (2005a). Two-layer flow behaviour and the effects of granular dilatancy in dam-break induced sheet-flow. *PhD thesis*. Department of Civil Engineering, Université Catholique de Louvain, Belgium.

Spinewine, B. (2005b). Two-layer shallow water modelling of fast geomorphic flows and experimental validation on idealized laboratory dam-break waves. Proc. 31st *IAHR Congress* Seoul 2, 1437–1439.

Spinewine, B., Zech, Y. (2007). Small-scale laboratory dam-break waves on movable beds. *J. Hydraulic Res.* 45(1), 73–86.

Stoker, J.J. (1957). *Water waves*. Wiley-Interscience, New York.

Toro, E.F. (2001). *Shock-capturing methods for free-surface shallow flows*. John Wiley & Sons, Chichester.

Wei, L. (1990). Governing equations for mathematical river modelling. In *River modelling*, J. Xie, ed. China Water Power Press, Beijing, 8–15 (in Chinese).

Wong, M., Parker, G. (2006). Reanalysis and correction of bed load relation of Meyer-Peter and Muller using their own database. *J. Hydraulic Eng.* 132(11), 1159–1168.

Wu, W., Wang, S. (2007). One-dimensional modeling of dam-break flow over movable beds. *J. Hydraulic Eng.* 133(1), 48–58.

Xia, J., Lin, B., Falconer, R.A., Wang, G. (2010). Modelling dam-break flows over mobile beds using a 2D coupled approach. *Adv. Water Res.* 33(2), 171–183.

Zech, Y., Soares-Frazão, S., Spinewine, B., Grelle, N. (2008). Dam-break induced sediment movement: Experimental approaches and numerical modelling. *J. Hydraulic Res.* 46(2), 176–190.

Zech, Y., Soares-Frazão, S., Spinewine, B., Savary, C., Goutière, L. (2009). Inertia effects in bed-load transport models. *Can. J. Civil Eng.* 36(10), 1587–1597.

Zhang, R., Xie, J. (1993). *Sedimentation research in China: Systematic selections*. China Water Power Press, Beijing (in Chinese).